Analysis of Photometric Observations
of the New Cataclysmic Variable ASASSN-13cx

T. S. Khruzina[1*], I. B. Voloshina[1**], S. Qian[2], and V. G. Metlov[1, 3]

*[1]Sternberg Astronomical Institute, Lomonosov Moscow State University,
Moscow, 119991 Russia*
*[2]Yunnan Observatories, Chinese Academy of Sciences,
P.O. Box 110, Kunming 65011, Yunnan, People's Republic of China*
[3]Lomonosov Moscow State University, Crimean Astronomical Station, Nauchnyi, Russia
Received August 4, 2017; in final form, September 5, 2017

Abstract—Photometric observations of the variable star ASASSN-13cx acquired in the course of a program of studies of cataclysmic variables and their parameters recently carried out at the Sternberg Astronomical Institute (SAI) are presented. The star was observed with the 50-cm and 60-cm telescopes of the SAI Crimean Astronomical Station and a CCD photometer ($\sim$1800 images in the V and Rc filters) during the variable's outburst of August−September 2014 and in a period of quiescence in October−November 2016. The ASASSN-13cx system is confirmed to be a SU UMa variable. Parameters of the system are derived from eight light curves using a "composite" model that takes into account the presence of a hot spot on the lateral surface of the geometrically thick disk and of a region of enhanced energy release near the disk edge, at the base of the gas flow (the so-called "hot line"). Parameters of the system for three light curves during the outburst were obtained in the framework of a "spiral" model that additionally takes into account the presence of geometric perturbations on the accretion-disk surface. The parameters of ASASSN-13cx determined using these models provide good accuracy in reproducing the system's light curves in both states. The basic parameters of the system have been determined for the first time: the component mass ratio $q = M_1/M_2 = 7.0 \pm 0.2$, the orbital inclination $i = 79.9°-80.1°$, the distance between the components' centers of mass $a_0 = 0.821(1)\,R_\odot$, and the sizes and temperatures of the stars: $R_1 = 0.0124(5)a_0 = 0.0102(4)\,R_\odot$, $T_1 = 12\,500 \pm 280$ K, $\langle R_2 \rangle = 0.236(4)a_0 = 0.194(3)\,R_\odot$, $T_2 = 2550 \pm 400$ K, corresponding to M4−9V for the spectral type of the secondary. Parameters of the accretion disk have been derived for both activity states. The mass of matter in the accretion disk increased by almost a factor of two during $\sim$400 orbital periods in quiescence.

1. INTRODUCTION

Cataclysmic variables—a highly populated class of close binary systems on the late evolutionary stages of their evolution—feature a wide variety of observed properties that provide a clear reflection of the various physical processes occurring in them. From this point of view, they represent an excellent laboratory for studying the physics of close binaries. The most striking observational features of these objects are their sudden brightenings by a large factor (outbursts), the appearance of new features in their light curves (dips, humps), and the considerable variations of the parameters of the companions in these systems.

Observations acquired during different states of the systems can be used in the framework of various models to derive numerical values of the parameters of the system. Comparison of such results makes it possible to obtain a better understanding of the essential nature of the processes occurring in cataclysmic variables (CVs), refine classifications of individual objects, and draw conclusions concerning the evolution of these systems.

The aim of our present study is to study the new CV ASASSN-13cx, recently discovered in the course of the ASASSN project and tentatively classified as an SU UMa dwarf nova. Our study includes analysis of detailed light curves of the system from our photometry of ASASSN-13cx in different activity states and determination of the parameters of its components. For completeness, we also used photometric observations from the AAVSO database.

The second section presents all the information on ASASSN-13cx published by the time of our study.

*[*]E-mail: `kts@sai.msu.ru`
*[**]E-mail: `vib@sai.msu.ru`
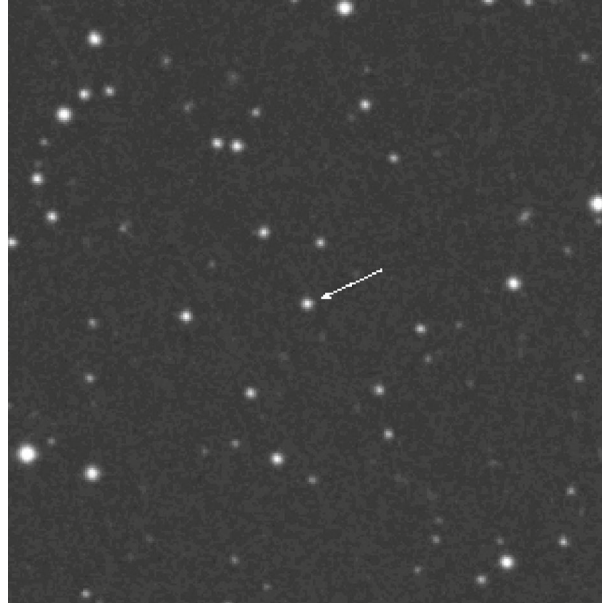
Fig. 1. Finding chart ($5' \times 5'$) for ASASSN–13cx (marked with an arrow).

Section 3 describes our own observations. Section 4 briefly introduces the main features of the models used to interpret the observed light curves, describes the model parameters, and presents estimates of the possible ranges of the basic system parameters. Section 5 is devoted to the results of our estimation of the system's basic parameters from an analysis of its quiescent light curve, while Section 6 considers other parameters of the close binary in the framework of a "composite" model for the light curves in quiescence and a "spiral-arm" model for the light curves during outburst. The results obtained are discussed in Section 7. Section 8 presents a summary of the main results obtained in our study.

2. INFORMATION ON ASASSN–13cx

The object ASASSN–13cx in the constellation Andromeda (see Fig. 1), with a brightness of $V = 15.47$, was discovered as a transient source on September 14, 2013 in the course of the ASASSN project. The object's other names are CMC15 J000222.3+424213, CSS J000222.4+424213, GSC2.3 NBGH007685, USNO−A2.0 1275−00025147, and USNO−B1.0 1327−0001011. The object has the equatorial coordinates $02^h02^m22.4^s$, $+42°42'14.2''$ and Galactic coordinates $l = 113.412°$ and $b = -19.259°$. Six earlier outbursts were recorded in the Catalina Real-time Transient Survey (CRTS) observations [1]. During the outburst that started on August 31, 2014 (JD 245 6901) [2], an international campaign to monitor the object was announced [3]. The observations during this campaign demonstrated that the ASASSN–13cx is apparently

an eclipsing binary and CV [4]. Figure 2, which displays light curves of the system in V and in white light (CV) covering an interval of about 12 nights, plotted using the AAVSO data, clearly demonstrates variations of the system's brightness level during the descending branch of the outburst in 2014 [5].

The orbital ephemeris of ASASSN–13cx was determined using observations obtained during this campaign [6]:

$$\mathrm{Min} = \mathrm{BJD}\ 245\ 6901.69823(5) \qquad (1)$$
$$+ 0.079650075(5)N.$$

The phase $\varphi = 0.0$ corresponds to an eclipse of the white dwarf.

As an example, Fig. 3 displays several individual V and white light (CV) light curves of ASASSN–13cx obtained by AAVSO observers, which clearly demonstrate variations of the light-curve shape similar to those observed for SU UMa systems. An analysis of out-of-eclipse brightness variations of ASASSN–13cx based on AAVSO data resulted in the following superhump periods [6]: $P_{1,\mathrm{sh}} = 0.083098(42)^d$ for the B stage and $P_{2,\mathrm{sh}} = 0.082647(35)^d$ for the C stage. The transition from the B stage to the C stage occurred on September 7, 2014. Since the A stage (ascending branch of an outburst) is always very short and difficult to observe, it was not possible to determine the superhump period for this stage. According to the CRTS observations, the mean superoutburst cycle is $\approx 350^d$, or half as long.

A new short-term brightness increase (outburst) of ASASSN–13cx, to 15.2^m, was detected on October 5, 2016 [7]; the V-band out-of-eclipse bright-
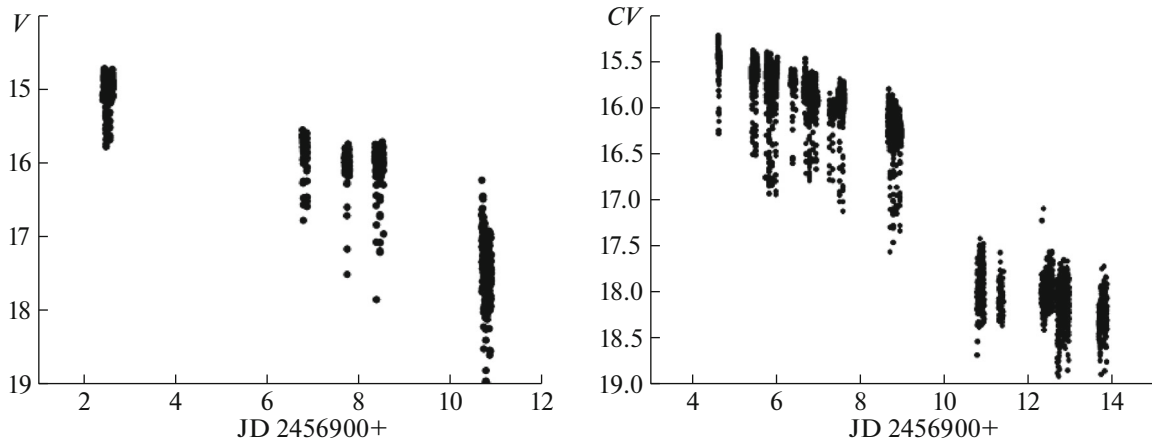
Fig. 2. AAVSO light curves of ASASSN-13cx during the descending branch of the outburst in August 2014 in *V* (left) and in white light, *CV* (right).
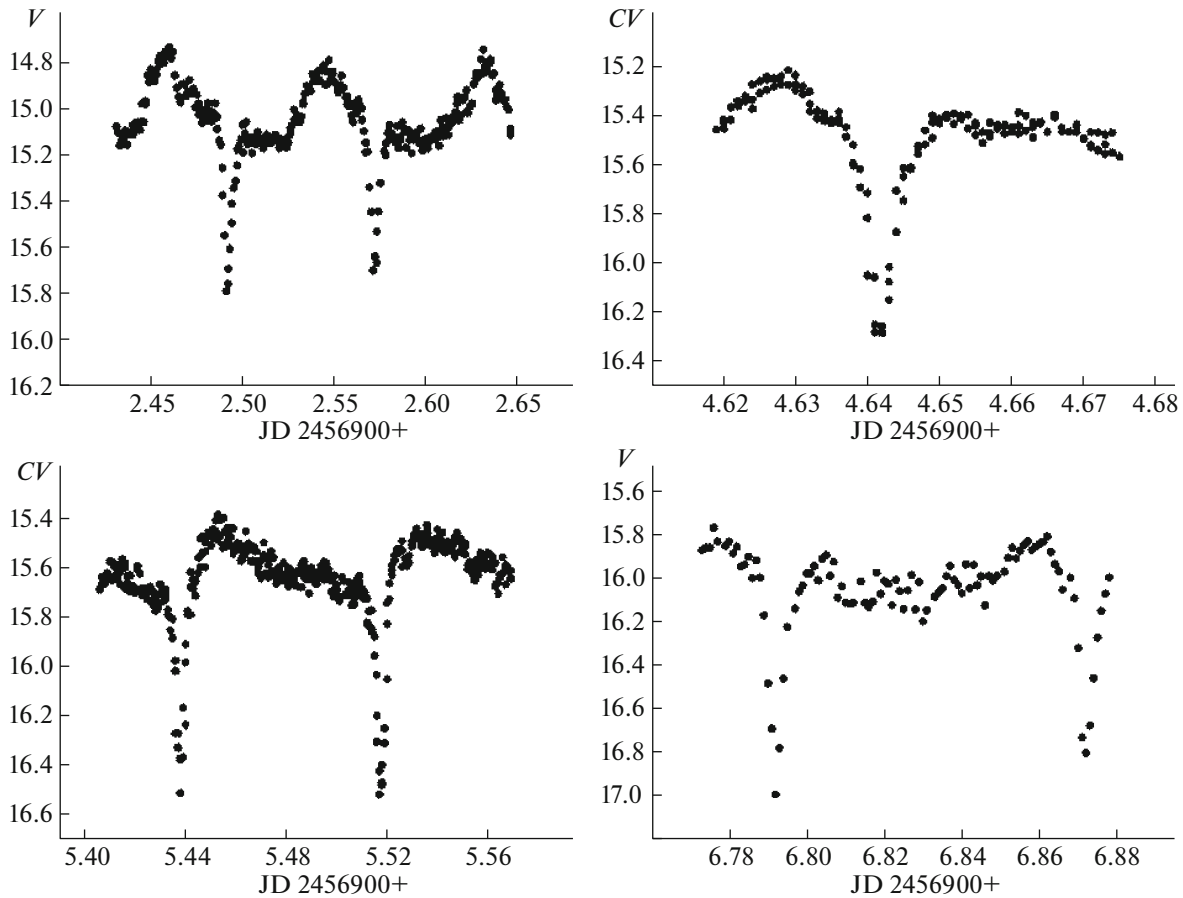
Fig. 3. Some of the individual light curves of ASASSN-13cx obtained in September 2014 by AAVSO observers in *V* filter and white light (*CV*).

ness of the object was 16.5^m and 18.2^m on October 9 and 14, respectively. By the beginning of our observations in the *Rc* filter (October 18, 2016), the out-of-eclipse brightness of ASASSN-13cx had already returned to its normal, post-outburst level, $Rc \sim 18^m$. In our observations of November 4, 2016 (JD 245 6697), we detected a short-term brightness increase by $\sim 1.5^m$; the flat shape of the out-of-eclipse part of the light curve indicated that the event was
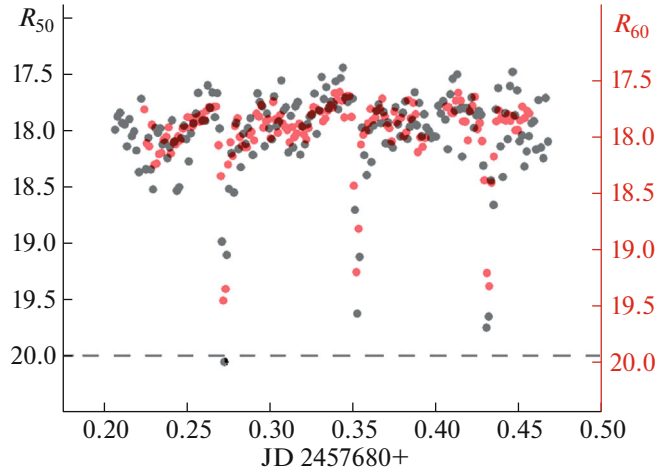
Fig. 4. Light curves of ASASSN-13cx obtained simultaneously on October 18, 2016 with the Zeiss-600 (red points, R_{60}) and AZT-5 (black points, R_{50}) telescopes in order to reveal instrumental differences.

due to a considerable increase in the light flux coming from the disk.

We observed ASASSN-13cx in the Rc band in the stage of brightness decrease during the September 2014 outburst and during a quiescent stage in October–November 2016. The light curves we obtained were used to determine the parameters of the system and to study the character of their variations in different activity stages.

3. OBSERVATIONS

We observed ASASSN-13cx with CCD photometers at the 50-cm and 60-cm telescopes of the Crimean Astronomical Station of the Lomonosov Moscow State University. The light detector used with the 50-cm telescope was an Apogee Alta U8300 CCD camera (3326×2504 pixels, 1 pixel = 5.4 μm) with a maximum efficiency of 60% at 5800–6600 Å and 30% near $\sim$4000 Å. With the 60-cm telescopes, we used an Apogee 47 CCD camera (1024×1024 pixels, 1 pixel = 13 μm). The durations of the observing runs were 4–7 hours, on average, in order to cover two to three orbital cycles of the binary, and depended on the weather. Since the sensitivity of the CCD detectors used was highest in the red, we observed in the Rc filter ($\lambda_c = 6700$ Å), close to the Johnson R band. The uncertainties of individual observations are approximately the same for both telescopes, $\sigma \sim 0.02$–0.06^m, depending on the weather conditions.

The comparison star is star No. 133 from the list of AAVSO standards, with brightnesses $B = 13.992 \pm 0.058$, $V = 13.320 \pm 0.029$, and $Rc = 12.922 \pm 0.061$ and coordinates $\alpha(2000) = 0^h02^m06.71^s$ and $\delta(2000) = +42°41'50.1''$, in the nearest vicinity of

ASASSN-13cx. We also observed several check stars in order to verify that the standard's brightness was constant. We reduced the observations using an aperture photometry technique with the MAXIM-DL software package.

ASASSN-13cx was observed on September 5–7, 2014 (JD 245 6906.3–6908.4), in the stage of brightness decline after a superoutburst maximum that occurred on August 31; overlapping AAVSO data are also present in this time interval (see Fig. 2). Our second series of observations of ASASSN-13cx was performed on October 18, 20, and 25, 2016 and on November 4, 17, 18, 19, and 22, 2016, after the return of the system's brightness to its quiescent level after the subsequent superoutburst, with its maximum brightness registered on October 5, 2016.

Our observations of ASASSN-13cx were obtained in the red (the Rc filter) on 11 nights; because the system is faint for the telescopes used, we obtained only one V light curve (on September 5, 2014), when the system was still comparatively bright, and it was not possible to obtain a quality V-band curve during quiescence. The exposure duration was 60 s on September 5, 2014 and 100 s on subsequent nights, as the variable faded towards the end of the outburst. A log of our observations is presented in Table 1.

Five of the 13 observing runs were obtained with the 50-cm AZT-5 telescope (September 5–7, 2014 and October 18, 2016): one of these was in the V band and four in the Rc filter. They correspond to the descending branch of the outburst and the first day of observations in quiescence. Eight observing runs in 2016 (quiescence, October 18–November 22) were obtained with the 60-cm Zeiss-600 (Zeiss-2) telescope; thus, two runs with the Rc filter were

Table 1. Log of observations of ASASSN-13cx

Date	JD 2450000+	Filter	n	$\varphi_b-\varphi_e$	Times of minima JD 2450000+	m_{min}	m_{max}	Telescope
2014.09.05	6906.404– 6906.490	V	108	0.138– 1.209	6906.473912	16.687	15.474	AZT-5
2014.09.05	6906.260– 6906.403	Rc	179	0.319– 1.119	6906.314050 6906.392962	16.316 16.174	15.217	AZT-5
2014.09.06	6907.242– 6907.450	Rc	162	0.654– 2.265	6907.269769 6907.349109 6907.428982	16.448 16.407 16.623	15.490	AZT-5
2014.09.07	6908.241– 6908.400	Rc	127	0.193– 2.194	6908.305474 6908.385405	16.794 16.798	15.517	AZT-5
2016.10.18	7680.224– 7680.457	Rc	154	0.380– 2.303	7680.272141 7680.352511 7680.432858	19.461 19.207 19.332	17.607	Zeiss-2, AZT-5
2016.10.20	7682.240– 7682.463	Rc	148	0.689– 2.481	7682.264699 7682.345092 7682.422569	19.191 19.589 19.819	17.445	Zeiss-2
2016.10.25	7687.217– 7687.533	Rc	219	0.178– 3.138	7687.281874 7687.362245 7687.441180 7687.521516	20.287 20.747 20.454 20.212	17.531	Zeiss-2
2016.11.04	7697.188– 7697.422	Rc	299	0.359– 4.289	7697.239178 7697.318981 7697.398009	17.441 17.532 17.715	16.056	Zeiss-2
2016.11.17	7710.307– 7710.421	Rc	76	0.059– 1.501	7710.382685	19.192	17.640	Zeiss-2
2016.11.18	7711.157– 7711.349	Rc	134	0.739– 4.152	7711.178773 7711.257673 7711.338020	19.685 19.131 19.302	17.574	Zeiss-2
2016.11.19	7712.363– 7712.450	Rc	128	0.877– 3.138	7712.372939 7712.453495 7712.532615	19.957 19.929 20.356	17.531	Zeiss-2
2016.11.22	7715.219– 7715.298	Rc	56	0.735– 1.726	7715.240625	18.600	17.212	Zeiss-2

n is the number of observations on a given night; φ_b and φ_e are the orbital phases at the beginning and end of the observations according to (1). The sixth column presents the observed times of brightness minimum for the given run.

obtained on October 18, 2016 with the two telescopes simultaneously. Comparing these observations indicated that reducing the fluxes (in magnitudes) obtained with the AZT-5 telescope in the Rc filter (Rc_{50}) to the Zeiss-600 instrumental system (Rc_{60}) requires the following correction:

$$Rc_{60} = Rc_{50} - 0.05^m. \qquad (2)$$

Figure 4 displays the two light curves of ASASSN-13cx obtained simultaneously with the two telescopes on October 18, 2016: the red data points are from the Zeiss-600 and the black ones from the AZT-5 telescope. This figure shows that the shifted curves are virtually identical in their overlapping parts. Our subsequent computations were performed for the Zeiss-600 instrumental system or for observations

reduced to it using Eq. (2), to obtain a homogeneous dataset. The similarity of light curves obtained with the two telescopes (taking into account the shift between them) was also clearly demonstrated in our earlier paper on observations of another CV, GY Cnc [8], also in the Rc filter.

Note the high level of out-of-eclipse flickering in Fig. 4. The situation for the other nights of observations of ASASSN-13cx is similar.

4. MODELS USED TO INTERPRET THE OBSERVATIONS. DESCRIPTION OF INPUT PARAMETERS

We used two different models to determine the parameters of the ASASSN-13cx system in different activity states more reliably.

1. A standard, "composite" model taking into account the presence of a hot line near the lateral surface of the disk and a hot spot on the disk, on the leeward side of the stream [9]. We used this model when analyzing the light curves in quiescence, assuming there were no geometric perturbations of the inner surface of the disk in this state.

2. A "spiral" model that schematically takes into account the presence of spiral waves in the disk, with the height of the wave crests dependent on the z coordinate of a point on the disk's surface, so that the crest height is largest near the disk edge and rapidly decreases towards the white dwarf [10].

4.1. Main Aspects of the Composite Model

The system consists of a spherical star (the primary) surrounded by a disk and a red dwarf (RD, secondary) that fills its Roche lobe. We subdivided the RD into 648 area elements that radiate in accordance with their own temperatures T_j, which depend on the star's effective temperature, T_2. When computing T_j, we took into account the heating of the RD surface by radiation from the inner regions of the accretion disk with the temperature T_{in}, $T_{in} > T_1$, where T_1 is the temperature of the primary. The shape and size of the secondary are determined by the component mass ratio, $q = M_1/M_2$. When computing the flux from an area element on the RD surface, we took into account gravitational darkening and limb darkening using a non-linear approximation.

The white dwarf (WD) primary is represented as a sphere of radius R_1 surrounded by a slightly elliptical accretion disk with an eccentricity $e \leq 0.25$, having its semi-major axis a at the azimuth α_e (where α_e is the angular distance in the orbital plane between the disk periastron and the line connecting the component centers of mass). The disk is optically thick and has a complex shape: it is geometrically thin near the

surface of the WD and geometrically thick at its outer edge, with an opening angle β_d. The temperature of each area element on the disk is given by $T(r) = T_{in}(R_{in}/r)^{\alpha_g}$, where R_{in} is the radius of the first orbit near the primary, $R_{in} \sim R_1$, T_{in} is the temperature of matter at the first orbit, and the parameter α_g is proportional to the viscosity of the gas in the disk. During the stationary state of the disk, $\alpha_g = 0.75$; as α_g decreases, the flux from the disk increases, due to the flatter radial distribution of the temperature in the disk. The computations of the local temperatures of selected areas on the disk took into account heating by high-temperature radiation from the disk's inner parts, as well as heating by radiation from the RD secondary (this effect, as a rule, insignificant).

Other radiating components are described in detail in [9]. Below we give a brief description in order to clarify the resulting parameters.

1. The region where the gas stream hits the disk is near the disk's lateral surface. The interaction between the stream and the disk is shockless; a shock appears in a narrow region along the edge of the stream (the "hot line," HL) as a result of the interaction of the incoming flows from the disk and the circumdisk halo with the stream material. As a result, the regions of energy release in this model consist of two regions on the surface of the HL, on its leeward and windward sides. We represent this emitting region of the HL with a truncated ellipsoid; the center of the ellipsoid (with the semi-axes a_v, b_v, c_v) is in the orbital plane, inside the disk. We computed the temperature distribution on the two sides of the HL independently; the distribution has a cosine law, with the corresponding temperature maxima at the line of intersection of the ellipsoid with the disk edge, $T_{ww,max}$ and $T_{lw,max}$ on the windward and leeward sides of the HL, respectively.

2. The hot spot (HS) on the lateral surface of the disk, on the leeward side of the stream. We represented this emitting area with a half-ellipse whose center U coincides with the point where the axis of the gas stream intersects the disk. R_{sp} is the radius of the ellipse in the orbital plane. Since part of the HS is obscured by the body of the gas stream, its actual size on the disk surface is smaller; however, the flux of light from the obscured part of the HS is compensated by regions of emission on the leeward side of the stream. The parameter β_{sp} determines the thickness of the disk's inner edge in the region of its interaction with the stream. This parameter is usually larger than the thickness of the disk's inner edge, β_d, in other parts.

The emission from all the components is blackbody radiation, and corresponds to the sum of the fluxes F_j from the area elements that are visible at the

given orbital phase. We computed the fluxes $F_j(T_i)$ using the Planck formula for the effective temperatures T_i corresponding to each of the area elements.

4.2. Main Aspects of the Spiral Model

We modeled the large-scale geometric perturbations near the outer edge of the disk (the "spiral arms") as geometric structures having the shape of two spiral-like arms in restricted range of azimuth, whose amplitude quickly decreases towards the inner regions of the disk. The method used to represent such a "perturbed" disk is described in detail in [10].

In general terms, we modeled the geometric perturbation on the inner paraboloid surface of the elliptical disk assuming that, when the center of an area of the disk with the coordinates (x, y, z) is inside the spiral arm, its z coordinate increases according to the formula

$$Z = z(x, y)h = z(x, y) \tag{3}$$
$$\times \frac{\zeta}{\sqrt{[r/R_d(\psi) - \exp(\psi - \eta - B)]^2 + 0.0025}}.$$

Formula (3) describes a spiral perturbation on the surface of the disk in restricted range of azimuth, explaining the name of the model. The coefficient ζ determines the amplitude of the wave; the angle ψ is the azimuth of the center of the area on the disk we are considering (x, y, z); η is the angle between the periastron of the slightly elliptical disk and the radius vector where the amplitude of the spiral reaches its maximum (the crest of the wave). The parameter B assumes the values 0 or 2π, depending on the position of the center of the area relative to the crest of the spiral arm. The second arm is at the position angles $\gamma + \eta > \psi > \eta$ (γ is the angular distance between the spiral-wave crests, $\gamma \sim \pi$). Since the amplitude of the logarithmic spiral is directly proportional to the z coordinate in the parabolic disk, it decreases very rapidly when approaching the white dwarf; as a result, only those parts of the spirals that are located in the outer parts of the disk appreciably influence the observed flux from the disk. For areas on the disk that are in the region of the spiral arms, the temperatures increase by a constant amount $\Delta T_{\rm spir}$, according to the expression $T_{\rm d,spir(i)} = T_{\rm d}(i) + \Delta T_{\rm spir}$, where $T_{\rm d}(i)$ is the area's temperature with no perturbation.

Thus, independent of the physical origins of the geometric inhomogeneities on the disk surface, our model makes it possible to take into account the influence on the close binary's light curve of the thickened outer edge of the disk within regions of restricted azimuth on its surface.

4.3. Estimating Possible Ranges of the System's Basic Parameters

Because of the complex structure of the disk during the outburst, the number of parameters in the spiral model is very large. The surface of the disk is not so perturbed during quiescence, making the number of unknown parameters in the composite model lower, but here we also obtained a considerable number of local minima of the residuals. Thus, it is important to restrict the region of allowed parameters for the system.

We used known statistical relations to estimate the ranges of possible values for the basic parameters of the CV: the radii and masses of its components and the distance between their centers of mass. We know:

(1) the binary's orbital period, $P_{\rm orb} = 0.079650075(5)^d = 1.9116$ hours,

(2) the superhump periods for stages B ($P_{1,\,\rm sh} = 0.083098(42)^d$) and C ($P_{2,\,\rm sh} = 0.082647(35)^d$),

(3) the period excess $\varepsilon = \dfrac{P_{\rm sh} - P_{\rm orb}}{P_{\rm orb}}$; in the case of ASASSN-13cx, this will be $\varepsilon_1 = 0.04329(53)$ for $P_{1,\,\rm sh}$ and $\varepsilon_2 = 0.03763(44)$ for $P_{2,\,\rm sh}$.

The component mass ratios in SU UMa systems are fairly high, usually $q = M_1/M_2 > 4$. A statistical relation between ε and $Q = M_2/M_1$ was derived in [11]: $Q = (0.114 \pm 0.005) + (3.97 \pm 0.41)(\varepsilon - 0.025)$. Taking into account all the uncertainties, we find $q \sim 5.0-5.81$, $\langle q \rangle = 5.36$ for ε_1 and $q \sim 5.67-6.56$, $\langle q \rangle = 6.10$ for ε_2. Thus, according to statistical expectations, the component mass ratio in the SU UMa variable ASASSN-13cx should be in the range $q \sim 5.0-6.6$. However, given the statistical character of this relation, we searched for the best-fit parameters in a wider range, $q \sim 5.0-7.5$.

According to [12], the empirical relations between the orbital period, $P_{\rm orb}$ (in hours), and the mass and radius of the secondary (in solar units) for $1.3 \leq P_{\rm orb} \leq 9^h$ can be expressed as $M_2 = 0.065 P_{\rm orb}^{1.25}$ and $R_2 = 0.094 P_{\rm orb}^{13/12}$. We obtain in the case of ASASSN-13cx $M_2 = 0.146 \ M_\odot$, $R_2 = 0.19 \ R_\odot$. Hence, from the selected range of q values, we obtain the *statistical* mass range for the WD $M_1 = (0.73-1.1) \ M_\odot$.

The WD radius can also be estimated from statistical relations. An analytical mass−radius expression for *cool* degenerate Hamada−Salpeter WDs [13] was obtained in [14]:

$$R_1 = 0.0112 \left[\left(\frac{M_1}{M_{\rm Ch}} \right)^{-2/3} - \left(\frac{M_1}{M_{\rm Ch}} \right)^{2/3} \right]^{0.5} R_\odot, \tag{4}$$

where $M_{\rm Ch} = 1.44\ M_\odot$ is the Chandrasekhar mass limit. We find for ASASSN-13cx, taking into account the uncertainties in the input data, $R_1 = (0.00673 - 0.01084)\ R_\odot$.

In the code used, the sizes of all the components were computed in units of the distance a_0 between the stars' centers of mass, rather than in solar radii. We can estimate a_0 from the Kepler's third law, written as

$$\frac{a_0}{R_\odot} = 4.2137 \sqrt[3]{\left(\frac{P_{\rm orb}}{1^d}\right)^2 \left(\frac{M_1 + M_2}{M_\odot}\right)}.$$

Using the M_1 and M_2 estimates obtained above, we find $a_0 = (0.746 - 0.839)\ R_\odot$.

Thus, the radius of the WD in relative units is in the range $R_1/a_0 \sim 0.0080 - 0.0145$. In units of ξ, where ξ is the distance between the inner Lagrange point and the WD center of mass (corresponding to $q \sim 5.4 - 7.5$ are $\xi/a_0 \sim 0.6655 - 0.6939$), the radius is $R_1/\xi \sim 0.012 - 0.022$.

5. DETERMINATION OF THE BASIC PARAMETERS OF THE BINARY

The basic parameters of a binary are the component mass ratio q (and in the ideal case, also the component masses M_1 and M_2) and the radius of the WD R_1 (the mean radius of the secondary is a function of q). The temperatures of the components are less dependent on the structure of the system. In the model used, the WD's temperature can be influenced by the irregular accretion of matter (the model assumes that a star's temperature is constant across its surface, so that an increase in the temperature of the matter at a local point on the stellar surface will appear as an increase in the mean temperature of the quasi-point source). The effective temperatures of red dwarfs are also far from constant, even for single stars.

Therefore, in order to restrict the domain covered by the basic parameters, we performed a detailed search for the basic parameters q, R_1, and i, as well as for the normalized flux (see below), in the composite model according to the following scheme.

1. We selected four mean quiescence light curves of ASASSN-13cx, each combining a sequence of two to four curves, in order to reduce the fluctuations along the mean curve; we chose four curves with the largest number of observations at the primary minimum, obtained on October 18, October 25, November 4, and November 18, 2016. We performed the procedures described below for each of these selected light curves.

2. We searched for the best-fit model parameters reproducing the selected light curve on a grid of q values in the range $5.0 - 7.5$, with the increment $\Delta q =$
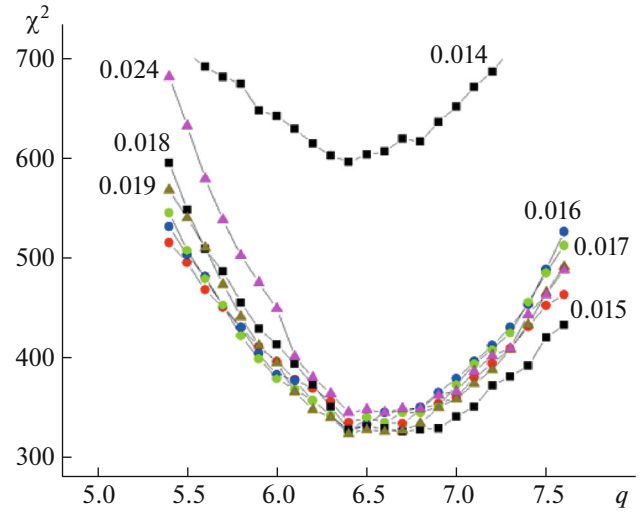
Fig. 5. $\chi^2(q)$ relations for a grid of R_1/ξ values (the numbers by the curves) obtained from an analysis of the binary light curve for the JD 687 run (October 25, 2016).

0.1, and a grid of R_1/ξ values in the range $0.010 - 0.024$, with the increment $\Delta R_1/\xi = 0.001$, for a wide range of initial values for the other binary parameters. Figure 5 displays a sample of such $\chi^2(q)$ relations for different values of R_1/ξ, obtained from the study of the mean light curve plotted from the observations of October 25, 2016.

For each value of q on the $(q,\ R_1/\xi)$ grid, we selected the set of parameters with the lowest χ^2 deviation. Figure 6a shows the resulting dependences of the minimum deviations on q for the four mean light curves listed above. Since the level of the deviations is different for the different light curves, we present the χ^2 values relative to the corresponding minimum value for the analyzed light curves, $\chi^2_{\min}$, $\chi^2/\chi^2_{\min}$.

The minimum for all the relations is $\chi^2/\chi^2_{\min} = 1.0$; we used the level 10% above the minimum, i.e., $\chi^2/\chi^2_{\min} = 1.1$, to estimate the range of acceptable component mass ratios. This yielded $q \sim 6.2 - 7.2$ for the light curves of October 18 and 25, 2016, $q \sim 6.8 - 7.6$ for November 4, and $q \sim 6.0 - 7.8$ for November 11, 2016. The region in common gives the estimate $q \sim 6.8 - 7.2$. The minimum deviations for the radius of the WD in this q range are $R_1/\xi \sim 0.016 - 0.022$ (October 18), $0.017 - 0.019$ (October 25), $0.016 - 0.020$ (November 4), and $0.017 - 0.021$ (November 11). We adopted $q = 7.0$ and $R_1/\xi = 0.018$ for our further computations.

3. Figure 6b shows the deviation versus the value of i used for the four light curves, with the same notation as in Fig. 6a. The range of allowed orbital inclinations, i, is fairly narrow for the light curve
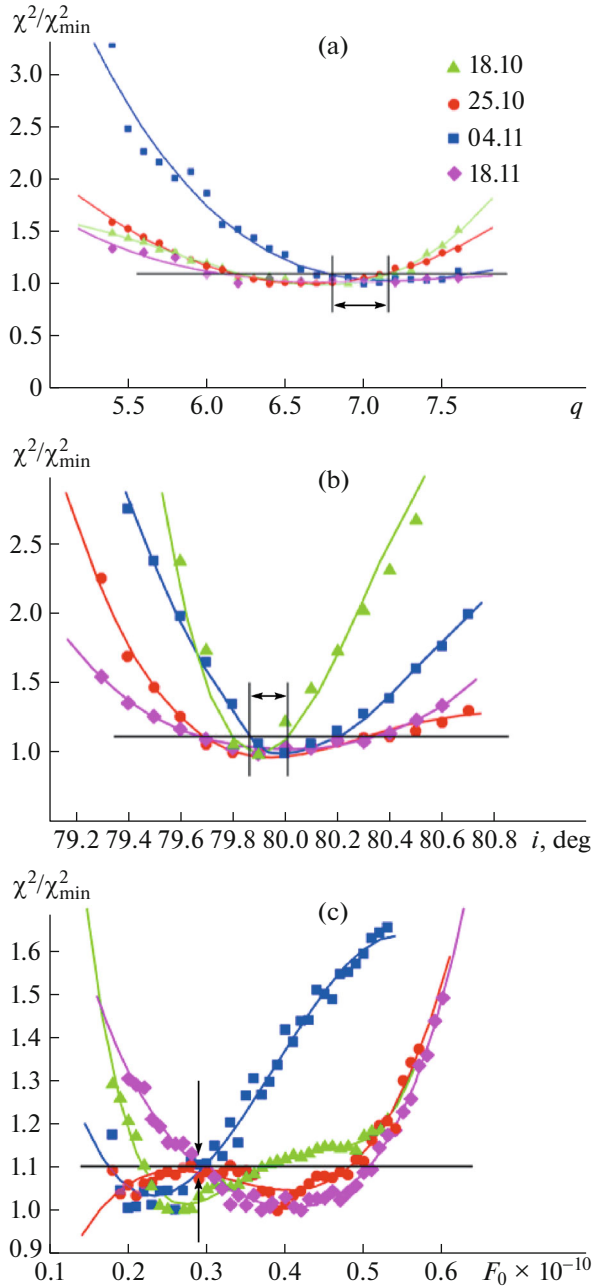
Fig. 6. Dependence of χ^2 normalized to the corresponding minimum value, χ^2_{min}, on (a) q, (b) i, and (c) F_0 for four light curves in quiescence (plotted using symbols of different colors and shapes). The curves in different colors are fits of the corresponding relations using third- and fourth-order polynomials. The horizontal lines mark the $\chi^2/\chi^2_{min} = 1.1$ levels. The short lines with arrows show the ranges of the corresponding parameters in common for the four curves at the $\chi^2/\chi^2_{min} = 1.1$ level.

of October 18, 2016, $i \sim 79.8°-80.0°$. This range is broader for the curve of November 4, 2016 ($i \sim 79.88°-80.22°$). For the remaining two light curves, the allowed interval at the 10% level are the same, $i \sim$

$79.7°-80.3°$. The intersection of the allowed intervals is $i = 79.88°-80.0°$, i.e., $i = 79.94° \pm 0.06°$, and our subsequent computations used the orbital inclination $i = 79.94°$.

4. Our light curves form a sequence of homogeneous curves, observed with the same equipment [after the correction according to (2)] and using the same comparison star. This enables us to additionally restrict the region of possible parameters. Namely, with the available sequence of several light curves, we translated the fluxes of the synthetic light curves into magnitudes using the same energy unit: the flux from the system corresponding to the same magnitude for all the light curves we used. In this case, when comparing the synthetic and observed light curves to determine parameter values, we can use both the shapes of the light curves and the variations of the radiation flux. We described this technique in detail in a number of our earlier publications (e.g., [15]).

Let us calculate the normalizing radiation flux F_0 for $Rc = 17.5^m$. For $q = 7.0$, $R_1/\xi = 0.018$, and $i = 79.94°$, the computed fluxes are in the range $F_0 \sim (0.19-0.50) \times 10^{-10}$ conditional units. We used conditional units here because the Planck function applied to compute the radiation flux from the area elements on the system's components per unit wavelength (in our case, in centimeters) is the energy flux through an area of 1 cm^2, and the unit of distance in the code is the distance between the binary components, a_0, which is unknown *a priori*. The results of our search for F_0 for each of the four curves, with q, R_1/ξ, and i fixed, are presented in Fig. 6c. The common interval below $1.1\chi^2/\chi^2_{min}$ for all four relations is near $F_0 \sim (0.29 \pm 0.03) \times 10^{-10}$ conditional units (marked with an arrow). We selected the mean value, $F_0 \sim 0.29 \times 10^{-10}$ conditional units, for our further computations.

5. The variations of the WD temperature, T_1, are not large, $T_1 \sim 12\,000-13\,000$ K, since the flux from the WD contributes very little to the combined flux from the system. In the code used, the disk surfaces and the areas on the secondary facing the WD undergo heating by hot radiation from the inner disk regions near the equator of the primary, with the temperature T_{in} (T_{in} is a parameter of the problem). Therefore, we did not perform a special search for this parameter, and took the mean value from the other searches, $T_1 = 12\,500$ K.

6. In the final stage, we searched for other parameters of the problem for all the light curves we had obtained (see Table 1), both in quiescence (the composite model) and during outburst (the spiral model), for the following basic parameters: $q = 7.0$, $i = 79.94°$, $R_1/\xi = 0.018$, $T_1 = 12\,500$ K, and $F_0 = 0.29 \times 10^{-10}$ conditional units (for $Rc = 17.5^m$).

6. PARAMETERS OF THE SYSTEM

We found the system parameters providing the shape of the synthetic light curve most closely matching the observed one applying the Nelder–Mead method [16]. When searching for the global minimum of the residuals for each of the light curves, we used several dozen different initial approximations, and several local minima were usually present in the studied parameter domain with a large number of independent variables. To estimate the agreement between the synthetic and observed light curves, we computed the residuals using the formula

$$\chi^2 = \sum_{j=1}^{J} \frac{(m_j^{\text{theor}} - m_j^{\text{obs}})^2}{\sigma_j^2}, \qquad (5)$$

where m_j^{theor} and m_j^{obs} are the magnitudes of the object at orbital phase j, obtained theoretically and from observations, σ_j is the dispersion of the observations at the jth data point, and J is the number of normal points in the mean light curve.

6.1. Quiescence

The results of our search for the parameters of the ASASSN-13cx system in quiescence are collected in Table 2. We estimated the uncertainties of the derived parameters by assuming a conditional limit for the residual for the given light curve, $\chi^2/\chi^2_{\min} = 1.1$. The uncertainties we obtained for the last one or two digits of each parameter are given in parantheses. The synthetic ASASSN-13cx light curves computed with these parameters are shown in Fig. 7. This figure is a square matrix; its first two "columns" (Panel I) contain eight light curves, observed and synthetic, while the other two columns (Panel II) present the contributions to the combined flux corresponding to these synthetic curves from different components of the system: (*1*) the WD, (*2*) the RD, (*3*) the accretion disk with a hot spot on its lateral surface, to the leeward side of the stream, and (*4*) the hot line on the surface of the truncated ellipsoid describing the shape of the stream near the disk edge. Table 3 presents the fluxes in conditional units from the ASASSN-13cx components at crucial points (minima, maxima, plateau) for the system light curves synthesized using the parameters from Table 2.

Bearing in mind the considerable flickering in the observations, there is satisfactory agreement between the theoretical and observed light curves. The flickering is considerably lower in the primary minimum than in out-of-eclipse parts of the light curves. The inserts in Fig. 7 (Panel I) show the theoretical light curves and unaveraged observations near the primary minimum (the three orbital phases marked along the

horizontal axis are $\varphi = 0.9$, 1.0, and 1.1). The agreement between the synthetic light curves and the observations is quite good here.

The quiescence light curves have variable amplitudes as well as shapes, indicating instability of the system at this stage. The light curves in the bottom row of Fig. 7 are especially striking. The observations for the night of JD 697 feature a considerable flare (by as much as $\sim 1.5^m$) due to an abrupt increase in the flux from the disk, compared to the other dates of our observations. The last light curve in the cycle (JD 715) exhibits an increased out-of-eclipse flux; it is, on average, $\sim 0.3^m$ brighter than the other six curves, while also having the lowest variation amplitude among the eight curves. This is also due to the fact that the flux from the disk is higher than for the other six light curves (see Fig. 7, Panel II).

Another noteworthy fact is that there is no plateau in the curves of the orbital variations of the flux from the disk for the nights of JD 711–715. Comparing the parameters of the disk for these dates to those obtained from observations on JD 680–697, we find that the disk was larger during the second half of the cycle than during the first half. The influence of other parameters is not so obvious.

Thus, we have confirmed our conclusion for other CVs we have studied earlier [8, 17, 18]: even in quiescence, there are factors causing variations of the accretion-disk parameters—its radius, temperature, and the character of its radial distribution.

6.2. Descending Branch of the Outburst

During the outburst, we obtained only three sets of observations in the Rc filter. Two of these feature an obvious "hump" in the region of orbital phases $\sim 0.4-0.6$; there is no hump at these phases in the third set (see Fig. 8). We applied the standard procedure used when searching for superhump periods. For each dataset, we determined the mean out-of-eclipse brightness (the eclipses of this binary are at phases $\Delta\varphi \sim 0.90-1.13$, we took a slightly broader range of eclipse phases) and calculated the deviations of the observations from the derived mean, ΔRc. We used the combined observations to derive a Fourier spectrum in order to independently determine the superhump period for a given part of the descending branch of the outburst. Figure 9 reproduces part of the spectrum. The maximum of the Fourier distribution corresponds to the period $P_{\text{sh}} = 0.08301(12)^d$, coinciding with the superhump period during the B stage [6], $P_{1,\text{sh}} = 0.083098(42)^d$, within the uncertainties.

Figure 10 shows the deviations ΔRc from the mean brightness for the corresponding date of observations, folded with the ephemeris:

$$\text{Max}\Delta Rc = \text{JD } 245\,6906.272 + 0.0830101E. \quad (6)$$

Table 2. Parameters of ASASSN-13cx in quiescence obtained from the analysis of light curves observed in 2016

Parameter	Oct. 18	Oct. 20*	Oct. 25	Nov. 11	Nov. 17	Nov. 18	Nov. 19	Nov. 22
JD 245 7000+	680.3	682.3	687.4	697.3	710.3	711.3	712.4	715.3
N	9775	9800	9864	9988	10152	10164	10178	10215
m_{max}	17.607	17.445	17.531	16.056	17.640	17.574	17.531	17.212
m_{min}	19.461	19.589	20.454	17.715	19.192	19.685	20.356	18.600
T_2, K	2650 ± 95	2665 ± 95	2363 ± 160	2570 ± 240	2575 ± 115	2570 ± 65	2375 ± 180	3095 ± 240
Accretion disk parameters								
e	0.09(2)	0.02(1)	0.03(3)	0.107(9)	0.024(6)	0.027(2)	0.019(4)	0.062(2)
$R_d(max)$, ξ	0.293(9)	0.301(3)	0.28(1)	0.350(5)	0.486(7)	0.463(2)	0.582(7)	0.537(4)
$R_d(min)$, a_0	0.167(9)	0.206(2)	0.18(1)	0.194(5)	0.319(7)	0.302(2)	0.386(7)	0.327(4)
$R_d(max)$, a_0	0.201(9)	0.207(2)	0.19(1)	0.241(5)	0.335(7)	0.319(2)	0.400(7)	0.370(4)
a, a_0	0.184(5)	0.207(2)	0.185(7)	0.218(3)	0.327(5)	0.310(1)	0.393(5)	0.348(3)
$0.5\beta_d$, deg	1.2(1)	1.7(1)	1.3(1)	0.7(1)	1.5(2)	1.36(2)	1.47(8)	1.32(4)
T_{in}, K	16 550 $\pm$ 160	15 485 $\pm$ 125	22 800 $\pm$ 445	31 295 $\pm$ 265	15 380 $\pm$ 255	15 460 $\pm$ 180	12 860 $\pm$ 260	14 840 $\pm$ 135
T_{out}, K	5540 ± 50	4750 ± 30	4540 ± 70	9110 ± 70	3420 ± 45	3665 ± 35	2850 ± 55	3955 ± 30
α_g	0.424(4)	0.473(4)	0.652(9)	0.437(4)	0.525(7)	0.512(4)	0.516(9)	0.438(3)
α_e, deg	118 ± 33	82 ± 30	62 ± 11	79.4(8)	68.0(5)	92.4(3)	57.2(5)	63.1(6)
Hot line parameters								
a_v/a_0	0.016(4)	0.028(1)	0.036(2)	0.021(2)	0.053(1)	0.0611(7)	0.082(3)	0.042(6)
b_v/a_0	0.34(2)	0.532(8)	0.467(25)	0.45(4)	0.360(1)	0.393(7)	0.360(8)	0.390(8)
c_v/a_0	0.0040(2)	0.0062(3)	0.0048(5)	0.0027(2)	0.0091(6)	0.0080(2)	0.0118(1)	0.0082(2)
$T_{ww,max}$, K	14 405 $\pm$ 1520	16 190 $\pm$ 2150	12 005 $\pm$ 1020	15 960 $\pm$ 1820	8670 $\pm$ 1955	9515 $\pm$ 1840	12 250 $\pm$ 100	9355 $\pm$ 855
$T_{lw,min}$, K	13 245 $\pm$ 280	14 510 $\pm$ 365	11 910 $\pm$ 350	16 315 $\pm$ 1090	15 355 $\pm$ 850	15 150 $\pm$ 300	13 665 $\pm$ 30	16 230 $\pm$ 530
Hot spot parameters								
R_{sp}, a_0	0.10(2)	0.17(2)	0.16(3)	0.14(5)	0.20(1)	0.19(1)	0.17(1)	0.189(4)
$0.5z_{sp}$, deg	2.2(2)	3.4(5)	2.6(3)	1.1(3)	1.5(1)	1.45(6)	2.0(2)	1.3(1)
χ^2	28.8	30.0	315	690	137	339	149	34.2

The following basic parameters were adopted: $q = M_1/M_2 = 7.0(2)$, $i = 79.94(24)°$, $R_1 = 0.0124(5)a_0 = 0.0180(5)\xi$, $\xi = 0.688(5)a_0$; $T_1 = 12\,500 \pm 280$ K, $\langle R_2 \rangle = 0.236(4)a_0$. N is the number of the orbital cycle according to the ephemeris (1). R_{sp} is the distance in the orbital plane between the HL axis and the outer edge of the hot spot. * The trend was taken into account when averaging the three orbital curves taken during the night.

Different symbols are used to show the observations obtained at different nights. The maximum of this relation corresponds to the clearly expressed hump in the first observing run.

The hump in the light curve for the third observing run (JD 908) also occurs at orbital phase $\sim$0.5, as for the first night of observations (JD 906). The time elapsed between these phases is $\sim 24P_{sh}$. The hump

Table 3. Fluxes from the components of ASASSN-13cx in 2016 in the Rc filters in conditional units obtained in the corresponding models for outburst and quiescence

Parameter	JD 906	JD 907	JD 908	JD 680	JD 682	JD 687	JD 697	JD 710	JD 711	JD 712	JD 715
	Outburst			Quiescence							
Red dwarf:											
Min $\varphi \sim 0.0$	0.46	0.54	0.61	0.10	0.08	0.04	0.08	0.08	0.08	0.04	0.34
$\varphi \sim 0.5$	2.86	1.62	3.19	0.11	0.08	0.15	0.75	0.09	0.08	0.03	0.30
Quadratures	~ 1.6[1]	~ 1.2[1]	~ 1.8[1]	0.16	0.12	0.16[1]	0.78[1]	0.12	0.12	0.06	0.47
White dwarf: 0.0 conv. units (minimum), 0.21 conv. units (out of eclipse)											
Accretion disk:											
Min $\varphi = 0.0$	8.41	6.92	4.97	0.38	0.35	0.11	2.65	0.31	0.29	0.10	0.66
Plateau $\varphi \sim 0.1-0.6$	20.21[2]	16.97[2]	12.90[2]	1.40	1.14	1.02	8.50				
Hump, $\varphi \sim 0.8$	18.13[3]	12.62[3]	10.1[3]	1.65	1.68	1.31	8.61	1.74	1.69	1.82	2.46
Hot line:											
Min $\varphi \sim 0.0$	0.0	0.0	0.0	0.0	0.0	0.0	0.0	0.0	0.0	0.0	0.0
Min $\varphi \sim 0.5$	0.0	0.0	0.38	0.12	0.07	0.39	0.57	0.04	0.02	0.0	0.03
Max $\varphi \sim 0.2$	0.73	0.28	1.71	0.43	0.40	0.82	0.83	0.06	0.10	0.04	0.08
Max $\varphi \sim 0.8$	1.57	1.14	2.12	0.38	0.57	0.85	1.16	0.42	0.37	0.03	0.47

[1] Strong reflection effect, no minimum at phase $\varphi \sim 0.5$.
[2] Flux in the region of the hump.
[3] No hump, the presented flux occurs before entering the eclipse.

for the second observing run (JD 907) is located near the eclipse or in the egress from eclipse: the maximum of the 13th cycle of the period P_{sh} (this is approximately the time between the humps in the first and second observing runs) is at orbital phase $\varphi \sim 0.04$.

Table 4 presents the system parameters we computed in the spiral model, which takes into account the presence of geometric inhomogeneities on the disk surface in the form of spiral arms, briefly described in Section 4.2. Figure 11 shows the synthetic light curves computed with these parameters (Figs. 11a, 11b), compared to the observations (Fig. 11a) and the mean light curves (Fig. 11b) in the V (top panel, JD 906) and Rc (other three panels, JD 906−908) filters. Given the strong fluctuations in the observed brightness, the agreement with the synthetic light curves is fairly good. Figure 11c shows the contributions of the radiation from the components of the system to the combined flux in conditional units. On all three dates, the main contribution to the combined flux is made by the accretion disk; this contribution is (see Table 3) 28 conditional units in V (JD 906); the contribution

from the disk in Rc decreases with time, being 20.2, 17, and 12.9 conditional units on JD 906, 907, and 908, respectively.

7. DISCUSSION

Figure 12 shows the time variations of several of the system parameters (plotted as a function of the number of orbital cycles N since the beginning of our observations): its Rc brightness, temperature of the secondary T_2, and characteristics of the accretion disk—its semi-major axis a, the temperature at its outer edge T_{out} and in the boundary layer T_{in}, the half-thickness of the outer edge of the disk $0.5\beta_d$, and the index α_g determining the radial distribution of the temperature. We show the parameters of the system during the descending branch of the outburst to the left of the vertical dashed line and the parameters in quiescence to the right of this line.

The out-of-eclipse Rc brightness of the system on the descending branch of the outburst was $\sim 15.5^m$, and the eclipse depth increased with time: 1.03^m on JD 906, 1.13^m on JD 907, and 1.28^m on JD 908.

Table 4. Parameters of ASASSN-13cx derived from light curves observed during outburst in September 2014

Parameter	5.09	5.09	6.09	7.09
JD 245 6000+	906.3	906.4	907.4	908.3
Filter	V	Rc	Rc	Rc
n	58	58	72	83
m_{max}	15.474*	15.167	15.440	15.467
m_{min}	16.687*	16.197	16.573	16.748
T_2, K	3190 ± 390	3106 ± 160	3175 ± 85	3230 ± 105
Accretion disk:				
e	0.098(3)	0.047(9)	0.023(3)	0.06(1)
R_d (max), ξ	0.447(2)	0.449(6)	0.400(3)	0.394(5)
R_d (min), a_0	0.253(1)	0.282(4)	0.263(2)	0.241(3)
R_d (max), a_0	0.307(1)	0.309(4)	0.275(2)	0.271(3)
a, a_0	0.280(1)	0.295(4)	0.269(2)	0.256(3)
$0.5\beta_d$, deg	0.86(1)	1.2(1)	4.0(1)	1.1(1)
T_{in}, K	$45\,830 \pm 470$	$39\,245 \pm 315$	$35\,025 \pm 165$	$39\,285 \pm 720$
T_{out}, K	8070 ± 85	7140 ± 60	6625 ± 30	7480 ± 70
α_g	0.558(4)	0.538(3)	0.542(2)	0.548(5)
α_e, deg	88(9)	85(6)	87.9(4)	86.5(4)
Hot line:				
a_v, a_0	0.099(2)	0.09(2)	0.15(4)	0.05(1)
b_v, a_0	0.36(2)	0.25(3)	0.20(2)	0.39(4)
c_v, a_0	0.004(1)	0.007(3)	0.034(8)	0.0056(4)
$T_{ww,max}$, K	$36\,930 \pm 10\,415$	$27\,890 \pm 16\,240$	$36\,045 \pm 15\,260$	$26\,735 \pm 6480$
$T_{lw,max}$, K	$18\,380 \pm 85$	$13\,215 \pm 60$	9405 ± 30	$14\,230 \pm 75$
Spiral waves:				
ζ	0.53(1)	0.39(1)	0.27(1)	0.41(3)
ΔT_{spir}, K	2360 ± 220	6710 ± 140	8615 ± 130	3880 ± 190
$T_{d,spir}$, K	$10\,430 \pm 305$	$13\,850 \pm 200$	$15\,240 \pm 160$	$11\,360 \pm 260$
Δ_1, deg	10(1)	11.6(9)	57.8(2)	6.8(3)
Δ_2, deg	186(4)	183(3)	248(1)	190(2)
χ^2	266	385	356	453

* Fluxes in the system of the AZT-5 (50-cm) telescope. The adopted basic parameters are: $q = M_1/M_2 = 7.0(2)$, $i = 79.94(8)°$, $R_1 = 0.0124(2)a_0 = 0.0180(2)\xi$, $\xi = 0.688(2)a_0$, $T_1 = 12\,500 \pm 160$ K, $\langle R_2 \rangle = 0.236(2)a_0$. Δ_1, Δ_2 are the angular distances between the spiral-arm crests and the line joining the system components (measured clockwise, from the disk periastron).
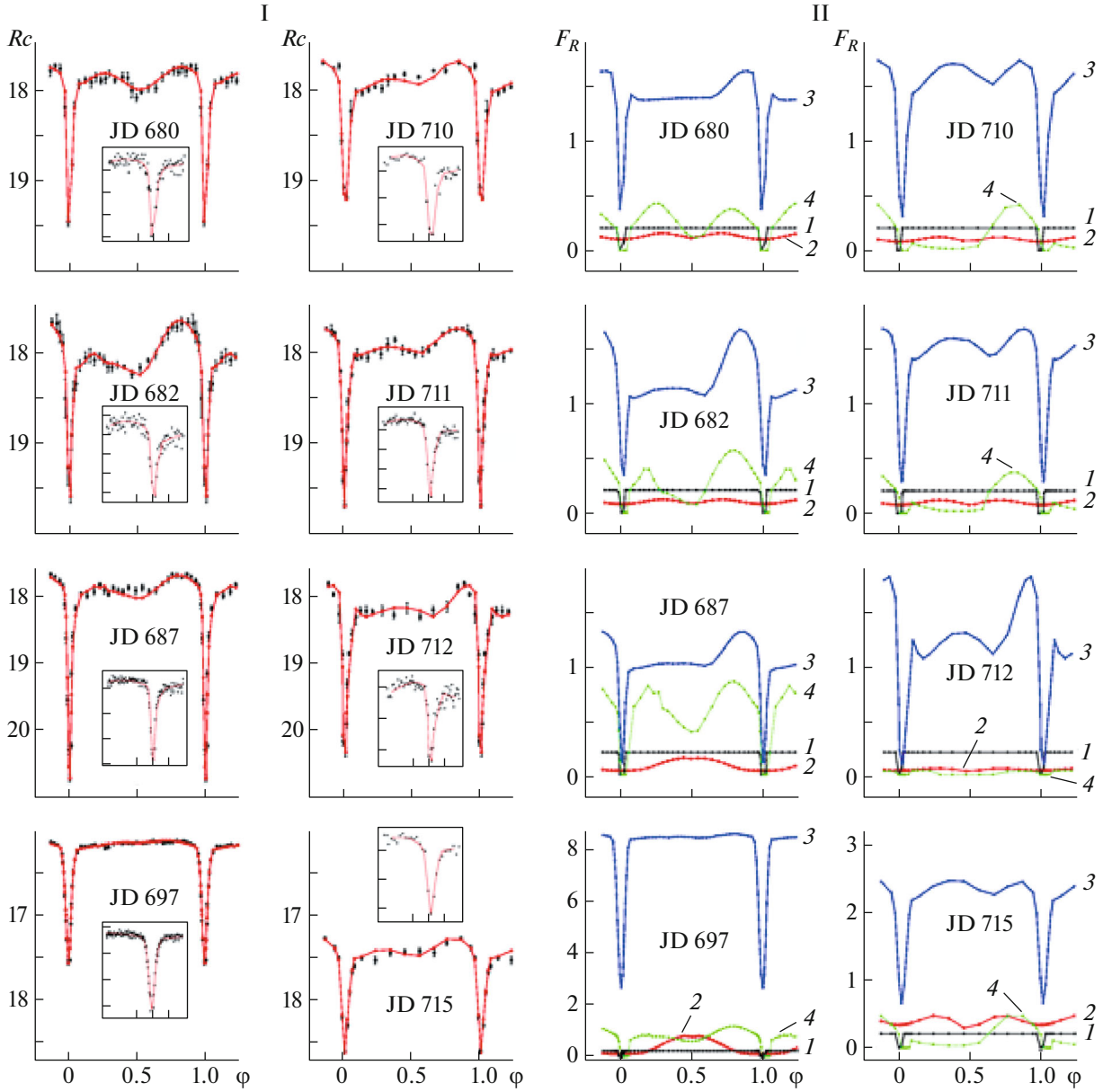
Fig. 7. Results of determining the ASASSN-13cx system parameters in quiescence. Left (Panel I): the mean light curves (points with error bars) and synthetic light curve for the parameters in Table 2 (colored solid curves). The inserts display the unaveraged observations and the synthetic light curves near orbital phases $\Delta\varphi = 0.9-1.1$. The marks along the vertical axes for the inserts are the same as those for the full light curves. Right (Panel II): contributions to the combined flux (in conditional units) from the system components: (1) the WD, (2) RD, (3) accretion disk with the hot spot on its lateral surface, and (4) hot line.

Our analysis of the visual (V and CV) AAVSO data (Fig. 2) shows that there is no obvious relation between the out-of-eclipse brightness level and the eclipse depth. After JD 910, the out-of-eclipse brightness level decreased by $\Delta CV \sim 1.8^m$; i.e., in terms of its brightness level, the system returned to quiescence. The out-of-eclipse Rc flux is not stable in the inactive state, being, on average, $Rc \sim 17.4-17.6^m$; in two of the eight observing runs, we

even recorded an increase in the Rc flux, to 16.1^m and 17.2^m for JD 698 and JD 715 (the bottom Panel I in Fig. 7). We do not observe any clear relation between the eclipse depth and the system's out-of-eclipse brightness level in our data. During the 440 orbital cycles N of our observations of the system in quiescence, we see some hints of variations on a timescale of $\sim 315N$.
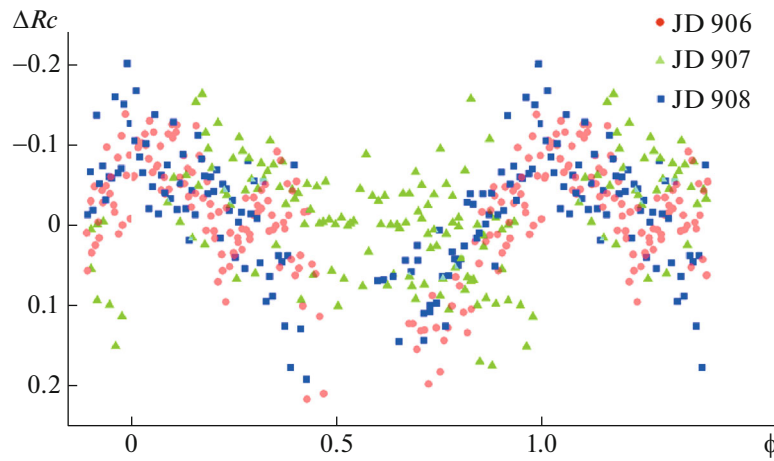
We did not fix the temperature of the secondary
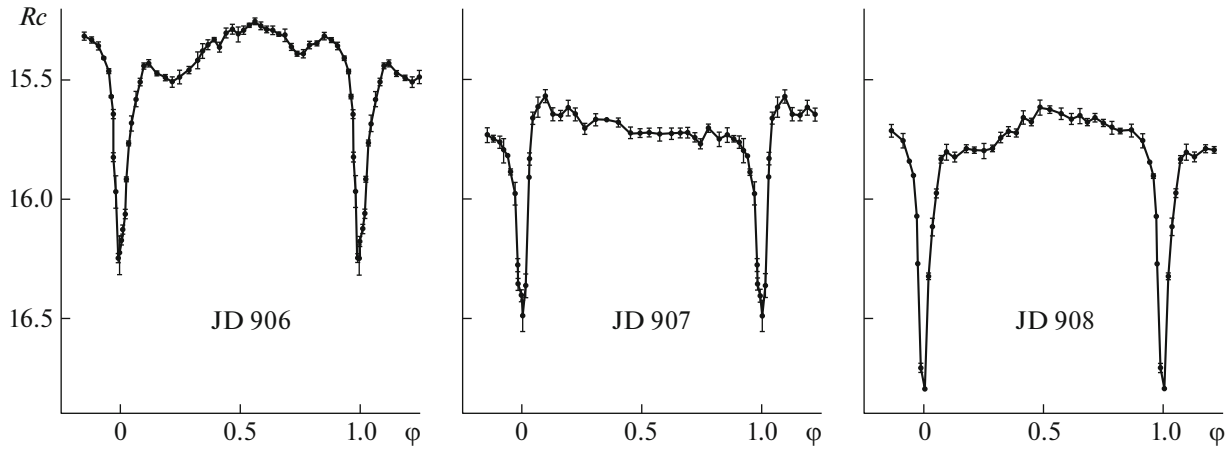
**Fig. 8.** Lignt curves of ASASSN-13cx observed during outburst in the Rc filter.
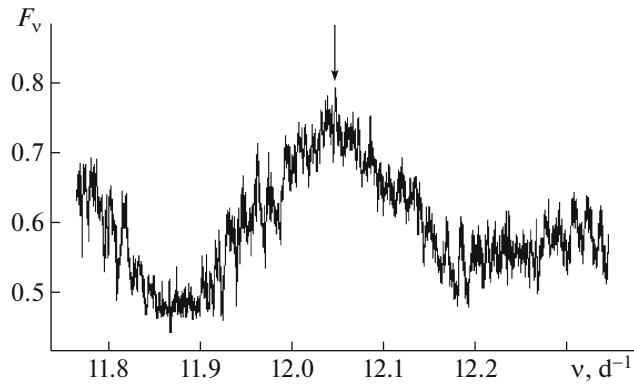
Fig. 9. Part of the Fourier spectrum for the region of the superhump period. The arrow marks the maximum of the frequency distribution corresponding to the period $P_{\rm sh} = 0.0830101^d$.


Fig. 10. The deviations ΔRc of the observations from the corresponding mean out-of-eclipse level for three runs during outburst (plotted as different symbols), folded with the ephemeris (6).
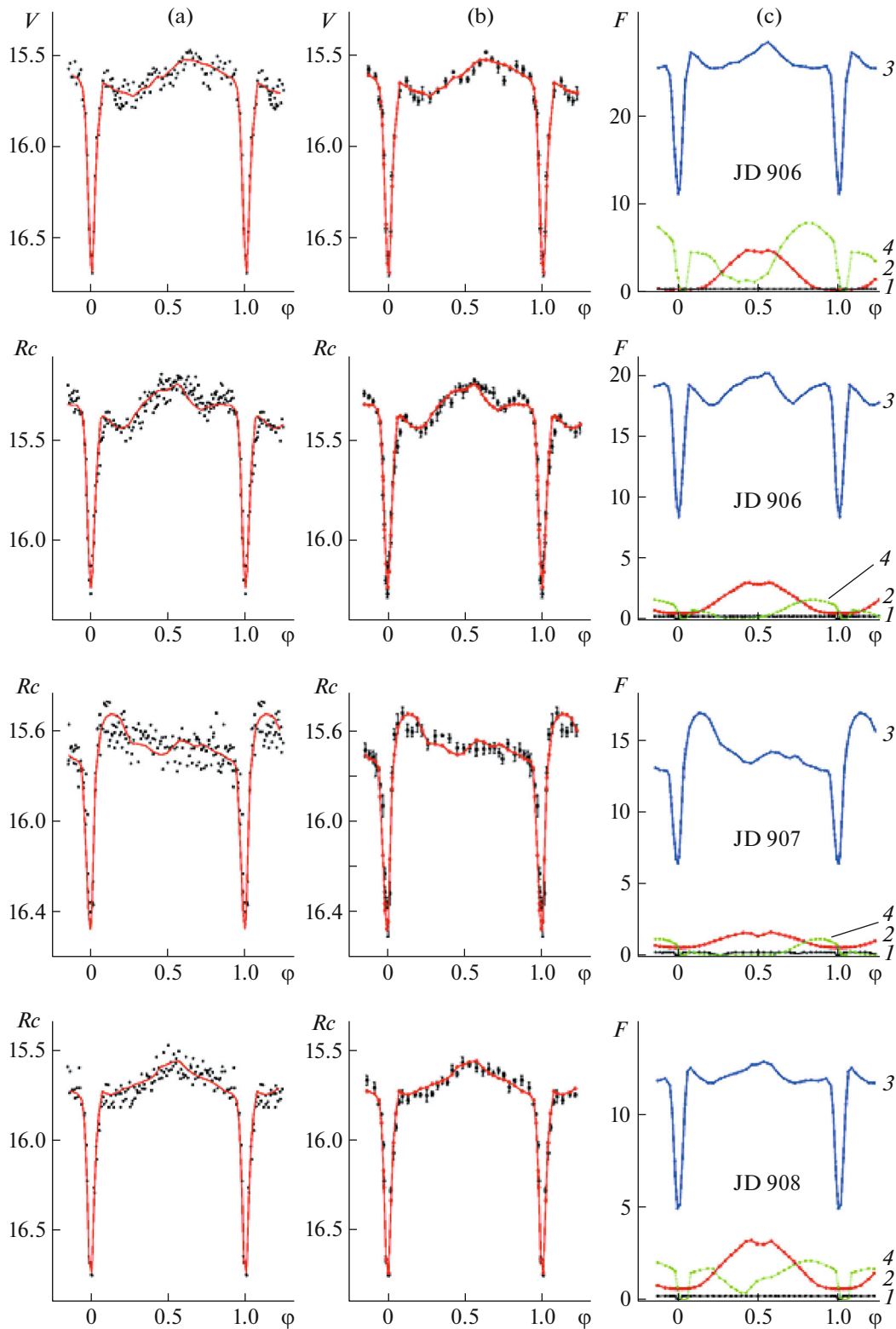
Fig. 11. Results of our determination of the ASASSN-13cx system parameters during outburst. The diagram shows the observations (points in panel (a), points with corresponding error bars on the mean curves (b)) and the synthetic light curves (solid colored curves) obtained using the parameters from Table 4, folded with the orbital period. The right panels (c) show the contributions from the system components to the combined flux (in conditional units): (*1*) the WD and (*2*) the RD, (*3*) the accretion disk with the spiral structure on its surface, and (*4*) the hot line.
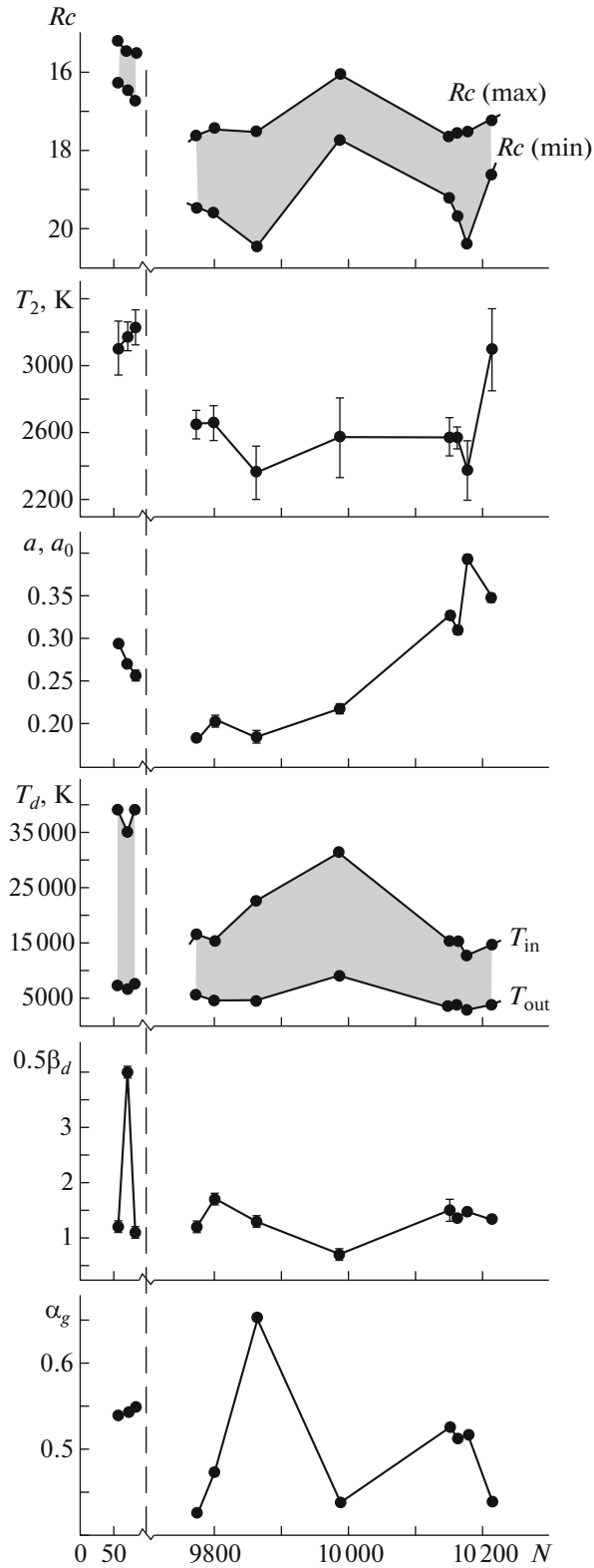
Fig. 12. Dependence on the orbital cycle number N (see Tables 4, 2) (from top to bottom) of the maximum and minimum flux from the system in the Rc filter (the variation amplitude is shown by gray shading), the effective temperature of the secondary T_2, the semi-major axis a of the elliptical accretion disk, the temperature in the disk boundary layer (T_{in}) and at the outer edge of the disk (T_{out}) (the variation amplitude is shown by gray shading), the half-thickness of the disk's outer edge (in degrees) $0.5\beta_d$, and the index α_{g}.

when determining the parameters, because this temperature can change with time, in particular, due to spot activity, as is often observed for late-type stars. During the outburst, $T_2 \sim 3200$ K, on average, while, out of outburst, $T_2 \sim 2550$ K; these temperatures are similar within the parameter uncertainties. The spectral type of the secondary can be estimated as M8 V (M4−9 V) according to [19]. This classification agrees well with the spectral types of secondaries in SU UMa CVs: according to [11, Fig. 7] the spectral type of the donor star corresponding to the orbital period $\sim 1.9^h$ is M6 V. The reflection effect is not strong, and becomes appreciable only for the observations on JD 697, when the flux from the disk had increased by almost a factor of eight compared to the other runs.

The accretion disk eccentricity is $e \leq 0.1$, in both outburst and quiescence (recall that $e^2 = 1 - b^2/a^2$, where a and b are the semi-major and semi-minor axes of the elliptical disk in the orbital plane, which has one of its foci at the center of mass of the WD). When $e = 0.1$, $b/a \approx 0.995$; i.e., the shape of the disk in the orbital plane differs only slightly from a circle. Note that Tables 2 and 4 contain the disk radius at periastron ($R_d(\min) = a(1 - e)$) and apoastron ($R_d(\max) = a(1 + e)$), creating the illusion of a non-circular disk in the case $e \sim 0.1$. Below, we use the term "disk radius" to mean the disk semi-major axis, a.

During the outburst, the disk radius varies insignificantly, decreasing from $\sim 0.3a_0$ to $0.26a_0$. In quiescence, we observed a systematic, almost twofold increase, from 0.18 to $(0.35-0.39)a_0$, during $\sim 400N$. Bearing in mind that the thickness of the disk edge does not change much in this process, $\beta_d \sim 2.6°$ (Fig. 12 shows the half-thickness of the disk edge, $0.5\beta_d$), its volume increases twofold during $\sim 400N$, clearly indicating the accumulation of matter in the body of the disk.

The temperature of the disk is determined by the temperature of the matter in its inner regions, near the WD, and the character of the radial temperature distribution, according to the expression $T_d(r) = T_{in}(R_{in}/r)^{\alpha_g}$. Assuming that each element of the disk emits as a blackbody, $\alpha_g = 0.75$ [20]. As the parameter α_g decreases, the matter in the disk generally becomes hotter. In the ASASSN-13cx system, α_g varies within $0.42-0.65$; during the outburst, $\alpha_g \sim 0.55$. Considerable variations of α_g occur on fairly short timescales, $\Delta t \leq 65N$. The general character of the variations of the temperature of matter in the boundary layer and at the outer edge of the disk repeats the character of the $R_d(\max)-R_d(\min)$ variations (see Fig. 12), with the same timescale; i.e., the variations of the disk parameters are the principal source of brightness variations of ASASSN-13cx.

Using the relations from Section 4.3 with $q = 7.0(2)$ and $M_2 = 0.146$ $M_\odot$, we find that the mass of the WD is $M_1 = 1.022(3)$ $M_\odot$. In this case, the distance between the component centers of mass is $a_0 = 0.821(1)$ $R_\odot$, the radius of the WD is $R_1 = 0.0102(4)$ $R_\odot$, and the mean radius of the secondary is $\langle R_2 \rangle = 0.194(3)$ $R_\odot$.

8. CONCLUSIONS

We have presented our new photometric observations of the eclipsing cataclysmic variable ASASSN-13cx, an SU UMa dwarf nova, during the descending branch following the outburst maximum in September 2014 and in a quiescent period in October−November 2016. We have performed a detailed analysis of the available observations. The light curves we obtained are in good agreement with observations from the AAVSO database.

We have determined the basic parameters of the system for the first time: the component mass ratio and orbital inclination ($q = M_1/M_2 = 7.0 \pm 0.2$, $i = 79.94° \pm 0.24°$), sizes and temperatures of the stars $R_1 = 0.0124(5)a_0 = 0.0102(4)R_\odot = 0.0180(5)\xi$, where $\xi = 0.688(5)a_0$ is the distance between the white dwarf's center of mass and the inner Lagrange point, $T_1 = 12\,500 \pm 280$ K; $\langle R_2 \rangle = 0.236(4)a_0 = 0.194(3)$ $R_\odot$, and $T_2 \sim 2550 \pm 400$ K. The distance between the component centers of mass is $a_0 = 0.821(1)$ $R_\odot$.

The spectral type of the secondary is estimated to be M4−9 V [19], in good agreement with the spectral types of secondaries in SU UMa cataclysmic variables.

According to [11], the main properties distinguishing SU UMa variables are a short orbital period, $P_{orb} < 2^h$ (in rare cases, $P_{orb} < 3^h$), the presence of "humps" in the orbital light curves that move with a period exceeding the orbital period by $1-5\%$ (in rare cases, up to 8%), and a high component mass ratio, $q > 4$. All these properties are also observed for ASASSN-13cx. The orbital period $P_{orb} = 1.9116^h$, the presence of superhumps in the system's light curves that move in orbital phases according to their period, $P_{sh} = 0.08301(12)^d$, the period excess $\varepsilon = 0.042(2)$, and the component mass ratio $q \sim 7$ all confirm that the ASASSN-13cx system is a SU UMa variable.

We have determined the parameters of the accretion disk (its radius, eccentricity, orientation, and the parameter α_g) on the descending branch of the outburst in September 2014 and in a period of quiescence in October−November 2016. Our analysis of variations of the disk parameters in this quiescent period, with a duration of $\sim 440N$, suggests the

presence of variations on a timescale of $\sim 315N$, and demonstrates that the main source of variations in the light curves of ASASSN-13cx is changes in the disk parameters. An almost twofold increase in the mass of matter in the disk occurred during the quiescent period analyzed, with a duration of $\sim 400N$. This was achieved due to a twofold increase in the disk radius, with the thickness of its outer edge showing little variation.

ACKNOWLEDGEMENTS

REFERENCES

1. A. J. Drake, S. G. Djorgovski, A. Mahabal, E. Beshore, et al., Astrophys. J. **696**, 870 (2009).
2. E. Muyllaert, CVnet-outburst, No. 6073 (2014).
3. T. Kato, VSNET-alert, No. 17682 (2014).
4. E. de Miguel and T. Kato, VSNET-alert, No. 17684 (2014).
5. S. Kafka, private commun. (2016).
6. T. Kato, F.-J. Hambsch, P. A. Dubovsky, I. Kudzej, et al., Astron. Soc. Jpn. **67**, 105 (2015).
7. T. Kato, VSNET-alert, No. 20215 (2016).
8. T. S. Khruzina, I. B. Voloshina, and V. G. Metlov, Astron. Rep. **60**, 971 (2016).
9. T. S. Khruzina, Astron. Rep. **55**, 425 (2011).
10. T. S. Khruzina, Astron. Rep. **49**, 783 (2005).
11. C. Knigge, Mon. Not. R. Astron. Soc. **373**, 484 (2006).
12. B. Warner, *Cataclysmic Variable Stars*, Vol. 28 of *Cambridge Astrophysics Series* (Cambridge Univ. Press, Cambridge, 1995), p. 111.
13. T. Hamada and E. E. Salpeter, Astrophys. J. **134**, 683 (1961).
14. M. Nauenbergs, Astrophys. J. **175**, 417 (1972).
15. T. S. Khruzina, A. M. Cherepashchuk, D. V. Bisikalo, A. A. Boyarchuk, and O. A. Kuznetsov, Astron. Rep. **47**, 214 (2003).
16. D. Himmelblau, *Applied Nonlinear Programming* (McGraw-Hill, New York, 1972).
17. T. S. Khruzina and I. B. Voloshina, Astron. Rep. **59**, 366 (2015).
18. T. S. Khruzina, P. Yu. Golysheva, N. A. Katysheva, S. Yu. Shugarov, and N. I. Shakura, Astron. Rep. **59**, 288 (2015).
19. G. M. H. J. Habets and J. R. W. Heintze, Astron. Astrophys. Suppl. Ser. **46**, 193 (1981).
20. N. I. Shakura and R. A. Sunyaev, Astron. Astrophys. **24**, 337 (1973).

Translated by N. Samus'